Jet Propulsion Laboratory
California Institute of Technology

Algorithm Theoretical Basis Document for OPERA Surface Displacement from Sentinel-1 data

Version 1.0.0
October 30, 2025
JPL D–108765

Revision A

Authors: Scott Staniewicz, Sara Mirzaee, Heresh Fattahi

National Aeronautics and
Space Administration
Jet Propulsion Laboratory
California Institute of Technology
Pasadena, California

Signature Page

Prepared by:

Approved via email. See email attachment in EPDM

Scott Staniewicz, OPERA ADT Engineer Date

Electronic Signatures in EPDM

Sara Mirzaee, OPERA ADT Engineer Date

Electronic Signatures in EPDM

Heresh Fattahi, OPERA ADT Engineer Date

Approved by:

Electronic Signatures in EPDM

Steven Chan, OPERA Project Scientist Date

Electronic Signatures in EPDM

Luca Cinquini, OPERA Project Manager Date

Electronic Signatures in EPDM:

Task	Status	Performer	Assignee Origin	Due Date	End Date
Document Approver List Approval : Signoff	Approve	Fattahi, Heresh (fattahi)	Document Approvers	26-Feb-2026 09:00	02-Mar-2026
Document Approver List Approval : Signoff	Approve	Chan, Steven K (chan)	Document Approvers	26-Feb-2026 09:00	02-Mar-2026
Document Approver List Approval : Signoff	Approve	Mirzaee, Sara (smirzaee)	Document Approvers	26-Feb-2026 09:00	17-Feb-2026
Document Approver List Approval : Signoff	Approve	Cinquini, Luca (cinquini)	Document Approvers	26-Feb-2026 09:00	17-Feb-2026

Document Change Log

Revision	Cover Date	Sections Changed	ECR #	Reason, ECR Title, LRS #
Initial, v0.1	June 15, 2023	All	N/A	New Document, LRR073167
Rev A, v1.0.0	Oct. 30, 2025	All	N/A	Revisions for changes going into production, LRR073167

TBD/TBC Log

Section	Description	Due Date

1 Introduction

The Earth's crust experiences ongoing displacements and deformations caused by natural and anthropogenic forces. Measuring and monitoring ground surface displacement plays a crucial role in hazard mitigation, infrastructure management, environmental monitoring, resource management, and geotechnical engineering, directly contributing to human safety, sustainability, and resilience [1]. Ground surface displacement caused by tectonic plate movements reveals the rate of strain accumulation at plate boundaries and helps in understanding the location and potential magnitude of future earthquakes [2, 3, 4]. Geodetic measurements of surface displacement caused by earthquakes can provide insight into the geometry, depth, slip, and mechanism of tectonic faults [5, 6, 7, 8]. Surface deformation near volcanoes may indicate changes in magma movements or accumulation, and increased uplift may signal potential volcanic eruptions [9]. Anthropogenic activities also cause significant ground displacement: groundwater extraction can lead to land subsidence with rates exceeding several centimeters per year in many urban areas worldwide [10, 11]; oil and gas production causes both subsidence from hydrocarbon extraction and uplift from fluid injection, with subsidence rates documented up to 5-10 cm/year in major producing fields [12, 13]; underground mining creates surface deformation bowls that can reach several meters of subsidence [14, 15]; and the impoundment of large reservoirs behind dams can trigger localized ground movements and reservoir-induced seismicity through increased pore pressure and crustal loading [16, 17]. Hence, continuous monitoring of ground surface displacement is a key factor in effective decision-making for the management and mitigation of both natural and human-induced hazards [1].

The National Aeronautics and Space Administration's (NASA) Observational Products for End-Users from Remote Sensing Analysis (OPERA) project [18, 19] provides timely, user-friendly surface displacement products derived from Sentinel-1 data (DISP-S1) at 30-meter spatial resolution with low latency for North America and its territories as one of the L3 level products in response to the needs identified by various federal agencies during 2018 cycle of the Satellite Needs Working Group (SNWG) [20]. DISP-S1 products are generated using Interferometric Synthetic Aperture Radar (InSAR), a technique that measures ground displacement by analyzing phase differences between two Synthetic Aperture Radar (SAR) Single Look Complex (SLC) images [1, 5]. These phase differences correspond to changes in distance between the radar sensor and ground targets. In repeat-pass interferometry, several factors influence the interferometric phase, including variations in radar viewing geometry between the two acquisitions, ground topography, atmospheric propagation delay, scattering properties of the targets, and surface displacement of targets[21]. While the geometric and topographic phase components can be modeled using knowledge of the satellite trajectories and existing Digital Elevation Models (DEMs) [1], other phase contributions are considered noise for displacement monitoring purposes [21].

A major source of error is temporal decorrelation, resulting from changes in the scattering surface properties over time [21]. Processes such as vegetation growth or loss, soil

moisture variations, and snowfall can significantly alter the land surface, leading to a loss of coherence. To mitigate these noise sources and enhance measurement reliability, modern InSAR approaches employ time-series analysis methods, processing stacks of multiple SAR acquisitions to derive surface displacement histories [22, 23].

InSAR time series algorithms may be broadly categorized based on the types of scatterers they include[24, 25]. Persistent Scatterer (PS) approaches identify stable radar returns over time, typically from strong reflective sources such as buildings or rocks [22]. Distributed Scatterer (DS) approaches average multiple pixels in areas assumed to have homogeneous scattering properties and deformation behavior [23]. PS approaches perform reliably in areas with strong reflectors (e.g., urban environments) but can have sparse spatial coverage [22]. Conversely, DS methods provide broader coverage but are more susceptible to decorrelation noise [23, 26].

InSAR time-series analysis for DS pixels can also be categorized based on the network of interferograms used to estimate the time series [25]. The Small BAseline Subset (SBAS) algorithm selects interferograms with short temporal and perpendicular baselines to maintain coherence [23, 27]. Alternatively, phase linking techniques use all possible interferometric pairs from a stack of SAR images to construct a covariance matrix [28, 29]. The covariance matrix serves as input to maximum likelihood estimation [29, 30] or eigenvalue decomposition algorithms [31] to estimate the wrapped phase time series. Although phase linking methods achieve high accuracy, their computational expense can be a notable drawback when processing hundreds of SLC images [30, 32] . The Sequential estimator [33] addresses some of the computational concerns by processing batches of SLCs at a time and creating compressed SLCs to summarize historical information. However, requiring an adjustment step [33] to previously archived products (i.e., "datum adjustment") introduces extra complexity that may be difficult for products archived at a Distributed Active Archive Center (DAAC). Hence, notable challenges still exist for creating an operationally-friendly time series algorithm and implementation capable of wide-area processing with low latency [24, 25].

This Algorithm Theoretical Basis Document (ATBD) describes the processing chain used by the OPERA project to generate Level 3 Surface Displacement from Sentinel-1 (DISP-S1) products. The DISP-S1 workflow includes PS selection, DS identification using Statistically Homogeneous Pixel (SHP) neighborhoods, wrapped phase estimation via phase linking on covariance matrices, interferogram generation, phase unwrapping, time-series inversion, and auxiliary correction layer calculations for ionospheric delays and solid Earth tides. The algorithm is optimized for efficient processing of the existing Sentinel-1 archive in "Historical mode" while also supporting "Forward mode" processing, where new displacement estimates are produced within the required 72-hour latency from the availability of all algorithm inputs. A key algorithmic contribution is a mini-stack reference scheme that maintains phase consistency across processing batches without datum adjustments, enabling straightforward operational deployment at continental scale.

2 DISP-S1 Algorithm

2.1 Background

The OPERA DISP-S1 algorithm generates displacement time series products from stacks of coregistered SLC images. A time series of Level 2 Sentinel-1 coregistered SLC (CSLC-S1) products covering the same area on the ground constitutes a stack of coregistered geocoded burst SLC images.

The algorithm operates in two distinct modes:

- **Historical mode**: Processes an existing archive of CSLC-S1 products to generate displacement outputs for all acquisition dates within each mini-stack. This mode is used for initial processing of the Sentinel-1 archive or for reprocessing existing data.
- **Forward mode**: Processes new CSLC-S1 acquisitions incrementally as they become available to generate near-real-time displacement products. This mode uses compressed CSLCs from previous processing runs to maintain phase continuity while only unwrapping a reduced network of interferograms for computational efficiency (see Section 2.12 for details).

The primary algorithmic difference between these modes is in the phase unwrapping step: Historical mode unwraps the full nearest-3 interferogram network ($3M - 6$ interferograms for M acquisitions), while Forward mode unwraps only the subset of interferograms connected to the newest acquisition (typically 6 interferograms), significantly reducing computational time.

Using the stack of CSLC-S1 products, the wrapped phase time series is estimated over PS and DS pixels at the desired output spacing. For PS pixels, the single-look phase is used directly. For DS pixels, the algorithm estimates the wrapped phase series using phase linking on the full covariance matrix computed from a statistically homogeneous pixel neighborhood. The estimated wrapped phase series are then unwrapped and converted to displacement with respect to a reference date and reference pixel.

Assuming that the observation vector of coregistered SLCs over time follows a complex circular Gaussian distribution, the coherence matrix can be used to estimate the wrapped phase series over an SHP neighborhood using a Maximum Likelihood Estimator (MLE) [28, 29] such as the phase triangulation algorithm (PTA) [30]. The wrapped phase series over DS pixels can also be estimated using classical eigenvalue decomposition (CED) [31], in which the wrapped phase series is derived from the eigenvector corresponding to the largest eigenvalue of the covariance matrix. Although MLE estimators are theoretically more accurate than CED, they are computationally more expensive. The eigenvalue decomposition-based maximum likelihood estimator (EMI) was shown to have estimation performance equivalent to other MLE estimators, while having stronger computational efficiency [32]. The EMI estimator requires the inverse of the coherence matrix, which may

not always be numerically stable. A combined eigenvalue maximum likelihood-based phase linking (CPL) first attempts to estimate the wrapped phase with EMI and, whenever the inverse of the coherence matrix cannot be computed due to numerical instability, the wrapped phase estimation falls back to the CED estimator [34].

2.2 Algorithm overview

The OPERA DISP-S1 near real time estimator processes a time-ordered stack of coregistered, geocoded SLC images to produce a wrapped phase history per output grid cell. Pixels dominated by a stable scatterer are designated as PS and retain single-pixel phases. Remaining pixels are treated as DS and are estimated from a SHP neighborhood using phase linking.

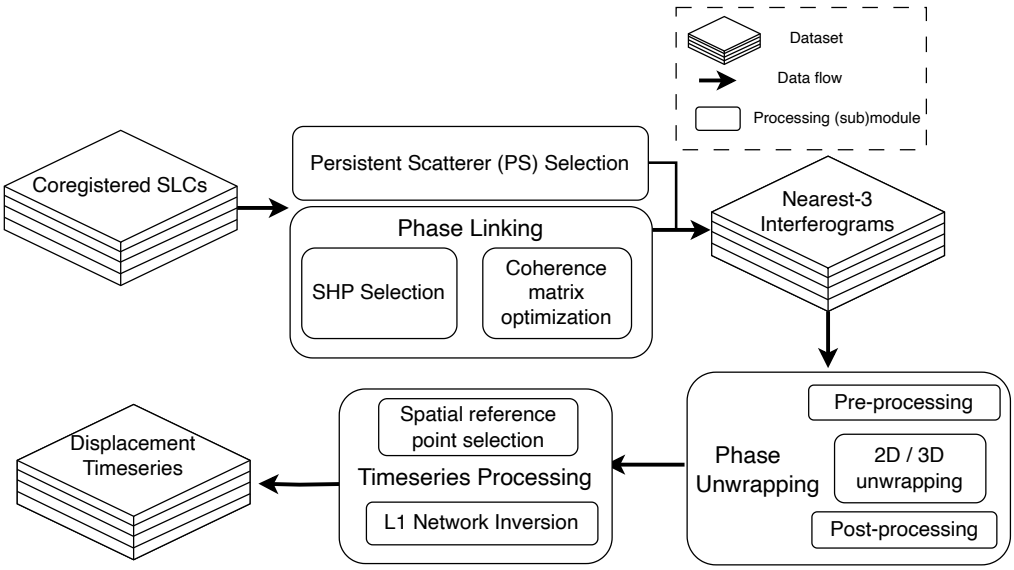

Figure 1: Summary of the processing modules used in the NRT InSAR phase estimation pipeline.

The incremental estimator uses a stack of M coregistered SLC images to perform time-series analysis and generate a single reference wrapped phase series from a full covariance matrix at the Sentinel-1 burst level. Given the apriori knowledge about the location of PS pixels, the estimated wrapped phase series at PS pixels are extracted to be the single reference interferograms without filtering or multi-looking. The bursts of wrapped phase series of PS and DS pixels are then stitched to form a predefined frame, unwrapped and converted to a displacement product. The DISP-S1 algorithm can be summarized into the following steps:

1. Select persistent scatterers (PS): The PS pixels are selected based on amplitude dispersion index.

2. Select distributed scatterers (DS): The DS pixels are selected using a statistical test on pre-computed amplitude mean and variance maps. DS pixels are further filtered based on quality indexes calculated in the next step.

3. Incremental phase linking: The wrapped phase series are estimated for DS pixels from a full covariance matrix.

4. Quality metrics: Using the results of the phase linking step, quality metrics are computed for the DS to filter out noisy regions.

5. Map PS and DS to 30 m resolution grid: Depending on the number of PS and DS in a decimation window, a decision is made to map them to a predefined lower resolution (30 m) by preserving PS pixels if they exist in that window.

6. Stitch bursts into frames: The wrapped phase series obtained in step 3 are burst-wise. They are then stitched to form a predefined frame for unwrapping in the next step.

7. Unwrapping: A network of the 3-nearest interferograms in time is created, and each interferogram is unwrapped independently using 2D phase unwrapping. 3D phase unwrapping is also available as an option; however, the 2D option was selected as it provides more coherent results across different study areas.

8. Time series inversion: The unwrapped interferogram network from the previous step is inverted and scaled to meters to create one displacement time series relative to the reference image used.

9. Corrections: For each displacement product, auxiliary correction layers are produced for ionospheric path delays and solid earth tides. These are not applied to the main layer, but may be applied by users who wish to use them.

The following subsections provide a detailed description of each step of the algorithm.

2.3 Selecting persistent scatterers (PS)

PS pixels contain a dominant, temporally stable scatterer whose phase is reliably observed at single-look resolution. Algorithm for identifying PS pixels generally fall into amplitude-based methods [22] or phase-based methods [35, 36]. Amplitude-based methods assume that when a pixel contains a strong dominant scatter, the noise contributions from other scatterers in the resolution element do not greatly affect the phase. At high SNR values, the phase standard deviation is approximately equal to the amplitude dispersion, D_A [22].

Following amplitude-based PS selection [22], we use the amplitude dispersion index

$$D_A \stackrel{\text{def}}{=} \frac{\sigma}{\mu} \tag{1}$$

where μ and σ are the mean and standard deviation of the amplitude time series at a pixel. Pixels with $D_A < \tau_{PS}$ where τ_{PS} is a predefined threshold, are labelled as PS. Our default choice of $\tau_{PS} = 0.2$ is conservative in the NRT setting to mitigate small-sample variability; amplitude moments (μ, σ^2) are computed using rolling statistics across mini-stacks to stabilize the estimate.

Two advantages of using D_A to select PS pixels are

1. The approach is very simple and fast to compute from a stack of CSLCs.
2. The mean and variance can be computed in an online manner by storing previously computed means and variances. This allows us to use many more images in estimating D_A than using only the current mini-stack of CSLCs.

Furthermore, the values of μ and σ^2 may be used during the selection of DS pixels, as explained in Section 2.4.

2.4 Selecting distributed scatterers (DS)

Pixels not classified as PS are treated as DS. For DS, phase noise is reduced by averaging over a neighborhood Ω of SHPs. To determine which neighboring pixels are homogeneous, statistical tests have been used on the coregistered stacks of CSLC amplitudes [30, 37]. Two of the most commonly used tests, the Kolmogorov-Smirnov (KS) test and the Anderson-Darling (AD) test, require the empirical cumulative distribution function (ECDF) which may be computed from N amplitude samples. Although these tests are non-parametric and flexible, there are two drawbacks of ECDF approaches:

1. The incremental processor which does not have access to large stacks, which makes the tests less powerful,
2. The computation of the ECDF involves sorting N values at every full-resolution CSLC pixel, which is computationally demanding.

To get around these limitations, we identify Ω using the generalized likelihood ratio test (GLRT), which only requires the mean and variance of each pixel's amplitude. [37].

Assuming circular complex Gaussian backscatter, CSLC amplitudes (A) follow a Rayleigh distribution:

$$p_A(A) \;=\; \frac{A}{s^2}\,\exp\!\left(-\frac{A^2}{2s^2}\right), \tag{2}$$

with scale parameter s. Testing homogeneity between pixels x and y reduces to

$$H_0 : s_x^2 = s_y^2, \tag{3}$$
$$H_1 : s_x^2 \neq s_y^2. \tag{4}$$

With N_x, N_y samples, the MLE is $\hat{s}^2 = \frac{1}{2N}\sum_{i=1}^{N} A_i^2$. Equivalently, if only (μ, σ^2) are stored, use $\hat{s}^2 = (\sigma^2 + \mu^2)/2$. The pooled estimate is count-weighted:

$$\hat{s}^2_{\text{pooled}} \;=\; \frac{N_x \hat{s}_x^2 + N_y \hat{s}_y^2}{N_x + N_y}.$$

The GLRT statistic derived from the log-likelihood is

$$T \;=\; 2\ln \hat{s}^2_{\text{pooled}} \;-\; \ln \hat{s}_x^2 \;-\; \ln \hat{s}_y^2. \tag{5}$$

Using Wilks' approximation [38], the test statistic T follows a chi-squared distribution with one degree of freedom ($T \sim \chi_1^2$) under the null hypothesis H_0. We accept homogeneity if $T \leq \chi^2_{1,1-\alpha}$ with a small false-alarm rate ($\alpha = 10^{-3}$). We evaluate candidates within a search window of ~ 200 meters and retain pixels passing the test to form Ω.

To support NRT processing, we maintain amplitude moments (μ, σ^2, N) across mini-stacks and update them with standard group-merge formulas:

$$\mu_{\text{new}} = \frac{\sum_i w_i \, \mu_i}{\sum_i w_i}, \tag{6}$$
$$\sigma^2_{\text{new}} = \frac{\sum_i w_i (\sigma_i^2 + \mu_i^2)}{\sum_i w_i} \;-\; \big(\mu_{\text{new}}\big)^2, \tag{7}$$

where μ_i, σ_i^2, and w_i are the amplitude mean, amplitude variance, and weight of each group. We use a simple even weighting across the existing previous 5 images.

2.5 Wrapped phase estimation for DS pixels

Phase linking estimates the wrapped phase evolution of a pixel from a stack of CSLC images. Let $\mathbf{z} \in \mathbb{C}^M$ be the CSLC vector over a mini-stack at a given output pixel, where M is the mini-stack size. We assume $\mathbf{z}$ arises from many independent scatterers in the resolution element (i.e., a distributed scatterer) and follows a circular complex Gaussian (CCG) distribution.

For each output pixel, we identify a SHP neighborhood Ω using the GLRT method (Section 2.4). Let $\{\mathbf{z}^{(l)}\}_{l=1}^{L}$ be the L samples from this neighborhood. We form the sample covariance matrix:

$$\widehat{\Sigma} \;=\; \frac{1}{L}\sum_{l=1}^{L} \mathbf{z}^{(l)} \big(\mathbf{z}^{(l)}\big)^H, \tag{8}$$

where $(\cdot)^H$ denotes the Hermitian (conjugate transpose) operator.

For convenience, we normalize each CSLC to unit average power, allowing $\widehat{\Sigma}$ to be treated as a coherence matrix with magnitudes ranging from 0 to 1.

The goal of phase linking is to recover a consistent set of optimal phase values $\hat{\boldsymbol{\theta}} = [\hat{\theta}_1, \ldots, \hat{\theta}_M]$ from $\widehat{\Sigma}$. Let $\hat{\boldsymbol{\zeta}} = [e^{j\hat{\theta}_1}, \ldots, e^{j\hat{\theta}_M}]$ denote the vector of unit-magnitude complex values corresponding to these phases. The maximum likelihood estimate solves the optimization problem [29, 30]:

$$\hat{\boldsymbol{\zeta}} = \arg\min_{\boldsymbol{\zeta}} \boldsymbol{\zeta}^H \Big(\Gamma^{-1} \circ \widehat{\Sigma} \Big) \boldsymbol{\zeta}, \tag{9}$$

where $\circ$ denotes the Hadamard (element-wise) product, and $|\zeta_i| = 1$ for all i.

Since the true coherence matrix Γ is unknown, we use $|\widehat{\Sigma}|^{-1}$ as an approximation to Γ^{-1}, where $|\cdot|$ denotes element-wise absolute value. We estimate the wrapped phase vector $\hat{\boldsymbol{\theta}}$ using the eigendecomposition-based maximum likelihood estimator (EMI) [32], which efficiently solves (9) as an eigenvalue problem:

$$\big(|\widehat{\Sigma}|^{-1} \circ \widehat{\Sigma} \big)\, \hat{\boldsymbol{\zeta}} \;=\; \lambda_{\min}\, \hat{\boldsymbol{\zeta}}. \tag{10}$$

The phase of the eigenvector corresponding to the smallest eigenvalue $\lambda_{\min}$ gives the phase-linking solution. We extract the phase estimates as $\hat{\boldsymbol{\theta}} = \angle\hat{\boldsymbol{\zeta}}$. At pixels where the inversion of $|\widehat{\Sigma}|$ fails due to numerical issues (typically at very high coherence pixels where many coherence magnitudes are near 1), we revert to the Eigenvalue Decomposition (EVD) method: we use the phase of the eigenvector corresponding to the largest eigenvalue of the sample coherence matrix $\widehat{\Sigma}$ [31]. This fallback strategy is implemented following the Combined Phase-linking approach [34].

Since we only need a single eigenvector (corresponding to $\lambda_{\min}$), we use the inverse power method [39], which is fast and effective for our typical small problem sizes of $M \approx 15 - 30$. Noting that eigenvalues of $|\widehat{\Sigma}|^{-1} \circ \widehat{\Sigma}$ all have magnitude greater than or equal to 1 [32], we set initial guess $\lambda_{\min}^{(0)} = 0.99$, and convergence typically requires fewer than 20 matrix multiplications per pixel.

Because interferometry measures only phase differences, one of the M phases in $\hat{\boldsymbol{\theta}}$ is not independently determinable. A reference index r must be chosen, and the referencing operation is performed by multiplying all elements of $\hat{\boldsymbol{\zeta}}$ by ζ_r^*, which sets $\hat{\theta}_r = 0$. Our choice of reference index for sequential processing is discussed in Section 2.6.

2.6 Compressed CSLCs and sequential batching

Modern SAR missions may acquire hundreds of images over a given region, making processing the full $N \times N$ covariance matrix computationally prohibitive. To limit computational cost while preserving long-baseline information, we partition the time series into smaller batches of size M, called *mini-stacks* [33]. Each mini-stack is processed to obtain a phase-linked estimate, which is then used to form a *compressed CSLC*, distilling the information in the mini-stack into a single complex image [40].

2.6.1 Compressed CSLC formation

Let $\hat{\boldsymbol{\zeta}} = e^{j\hat{\boldsymbol{\theta}}} \in \mathbb{C}^M$ be a unit-magnitude complex vector with the phase-linking solution for a mini-stack of M images. At each pixel, the compressed CSLC pixel $\kappa \in \mathbb{C}$ is formed by projecting the original CSLC vector $\mathbf{z}$ onto the phase-linking solution:

$$\kappa = \langle \hat{\boldsymbol{\zeta}}, \mathbf{z} \rangle = \hat{\boldsymbol{\zeta}}^H \mathbf{z}. \tag{11}$$

Writing $z_i = a_i\, e^{j\phi_i}$ and $\hat{\zeta}_i = e^{j\hat{\theta}_i}$, we can show that any chosen reference phase $\hat{\theta}_r$ factors out of this inner product:

$$\begin{aligned} \kappa &= \sum_{i=1}^{M} a_i\, e^{j\phi_i} \left(e^{j\hat{\theta}_i}\right)^* e^{j\hat{\theta}_r} \\ &= e^{j\hat{\theta}_r} \sum_{i=1}^{M} a_i\, e^{j(\phi_i - \hat{\theta}_i)}. \end{aligned} \tag{12}$$

Thus, each compressed CSLC pixel has a "base phase" from the reference $\hat{\theta}_r$, plus a weighted sum of the residuals between the true phases and the phase linking solution. This base phase property is critical for maintaining phase consistency across sequential mini-stacks.

2.6.2 Sequential processing scheme

We denote a compressed CSLC with reference phase $\hat{\theta}_r$ created from the mini-stack containing images i through $i+M-1$ as $\kappa^{(r)}_{i \to i+M-1}$. In our sequential batch processing scheme, the compressed CSLC from one mini-stack is prepended to the next mini-stack, increasing each mini-stack's size by one. This allows the formation of longer effective interferograms (reducing displacement bias from short-lived phase signals like soil moisture [41]) while reducing total computational cost by shrinking the size of the covariance matrix.

The OPERA DISP-S1 processing uses a modified sequential scheme designed to enable separate batch processing without requiring access to previous mini-stack outputs. The key difference from the scheme presented in the main journal paper [33] is the choice of reference index for each mini-stack. Rather than referencing to the first acquisition date of the archive, we reference each mini-stack to the *last real CSLC* in that mini-stack. This strategy is illustrated in Figure 2.

The processing proceeds as follows:

1. **First Mini-stack** ($\{z_1, \ldots, z_M\}$):
   (a) Perform phase linking with reference index $r = M$ (the last CSLC) to get $\hat{\boldsymbol{\zeta}}^{(1)}$.
   (b) Form compressed CSLC $\kappa^{(M)}_{1 \to M}$ using (11).

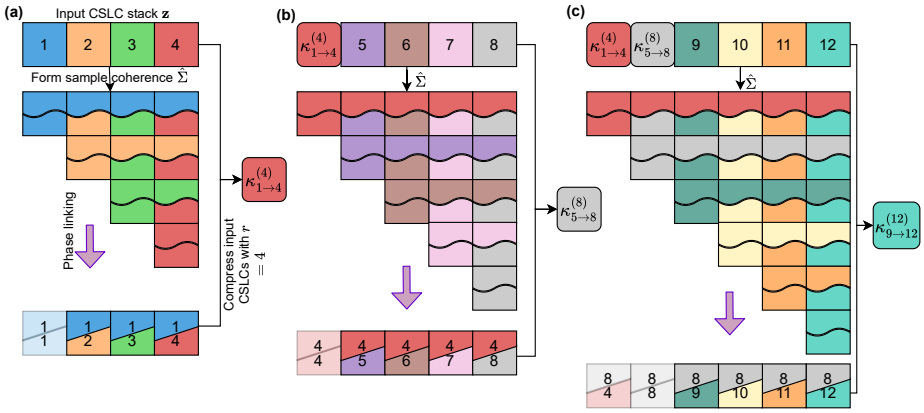

Figure 2: Sequential phase linking scheme used in OPERA processing to create short-temporal baseline mini-stacks with separate processing runs. (a) The first mini-stack (images 1-4) is phase-linked with reference index $r = 4$, and input CSLCs are compressed to produce $\kappa^{(4)}_{1\to4}$. (b) The second mini-stack uses $\kappa^{(4)}_{1\to4}$ as the first element. After phase linking with the compressed CSLC as reference, a new compressed CSLC $\kappa^{(8)}_{5\to8}$ is formed from the real CSLCs 5-8, referenced to CSLC 8. (c) Each subsequent mini-stack uses the most recent compressed CSLC as its first element and references phase linking to this compressed CSLC, then creates a new compressed CSLC from the real CSLCs referenced to the last real CSLC in the mini-stack.

2. **Second Mini-stack** ($\{\kappa^{(M)}_{1\to M}, z_{M+1}, \ldots, z_{2M}\}$):
   (a) Use $\kappa^{(M)}_{1\to M}$ (which has base phase $\hat{\theta}_M$ from the first mini-stack) as the first element.
   (b) Perform phase linking with reference index $r = 1$ (which corresponds to the compressed CSLC $\kappa^{(M)}_{1\to M}$).
   (c) Form new compressed CSLC $\kappa^{(2M)}_{M+1\to 2M}$ by projecting only the real CSLCs $\{z_{M+1}, \ldots, z_{2M}\}$ onto the phase-linking solution, with reference index $r = M$ (corresponding to the last real CSLC, z_{2M}).
3. **Third and Subsequent Mini-stacks**:
   (a) Prepend the most recent compressed CSLC to the new mini-stack.
   (b) Use the compressed CSLC as the reference for phase linking.
   (c) Form a new compressed CSLC from the real CSLCs only, referenced to the last real CSLC in the mini-stack.

By referencing each mini-stack to its last real CSLC, subsequent mini-stacks can form interferograms with the shortest possible temporal baselines. This would not be possible otherwise for the data processing system, which only has access to the current M CSLC-S1 products and to the k most recent compressed CSLCs.

The trade-off is that final displacement outputs cannot be directly referenced to the first date of the archive without combining results from consecutive mini-stacks. For the OPERA DISP-S1 product, users who wish to reconstruct the full displacement time series can concatenate consecutive mini-stack results using the overlapping reference dates. This trade-off was deemed acceptable to optimize for rapid displacement events (such as volcanic eruptions and landslides) while enabling efficient operational processing.

2.7 Quality of the estimated wrapped phase

The quality of phase-linked distributed scatterer (DS) pixels is commonly assessed using the *temporal coherence* γ_t [42], defined as:

$$\gamma_t \;=\; \frac{1}{N_{\text{ifg}}} \left| \sum_{i=1}^{M} \sum_{k=i+1}^{M} \exp\Big\{ j\big(\phi_{i,k} - \hat{\theta}_{i,k}\big) \Big\} \right|, \tag{13}$$

where $N_{\text{ifg}} = \frac{M(M-1)}{2}$ is the total number of interferograms, and $\phi_{i,k}$ and $\hat{\theta}_{i,k}$ represent the phase differences between the ith and kth images for the original interferometric phase and linked phase, respectively. This metric, also known as "goodness of fit" γ_{PTA} [30] or "a posteriori coherence" γ_{apt} [32], quantifies how well the estimated phases match the original observations.

While γ_t is effective for batch processing, it has limitations when applied to smaller mini-stacks. For $M = 2$ images, it always yields $\gamma_t = 1$, and for $M < 20$, its limited dynamic range makes it difficult to distinguish between high- and low-quality pixels.

To address these limitations, we also compute a complementary metric based on the cosine similarity measure [43]. For two vectors $\mathbf{x}$ and $\mathbf{y}$ of length K, the real-valued cosine similarity is:

$$s_{\mathbf{x},\mathbf{y}} \;=\; \frac{1}{K} \sum_{i=1}^{K} \cos\big(x_i - y_i\big). \tag{14}$$

We extend this concept to InSAR phase data by considering a search window W of radius r (typically $\sim 200\,\text{m}$) meters around each pixel. For a given pixel with phase-linked estimate $\hat{\boldsymbol{\phi}}$, we compute its phase similarity with each neighboring pixel $\mathbf{x}$ in W:

$$s_{\hat{\boldsymbol{\phi}},\,\mathbf{x}} \;=\; \frac{1}{N_{\text{ifg}}} \sum_{i=1}^{N_{\text{ifg}}} \cos\Big(\hat{\phi}_i \;-\; x_i \Big), \tag{15}$$

where x_i is the phase of image i at the neighboring pixel, and N_{ifg} is the number of re-formed interferograms that will be unwrapped. The *phase cosine similarity* γ_s is then defined as

the median of these similarities:

$$\gamma_s \;=\; \text{median}_{\mathbf{x}\in W}\left\{s_{\hat{\phi},\mathbf{x}}\right\}. \tag{16}$$

The γ_s metric measures how well a pixel's optimized phase history matches the neighboring pixels in space. Higher values indicate better agreement with local phase patterns. The median operation makes it more robust even with small CSLC stack sizes, and it provides a measure of pixel quality complementary to γ_t.

2.8 Approach to mapping PS and DS to 30 m resolution grid

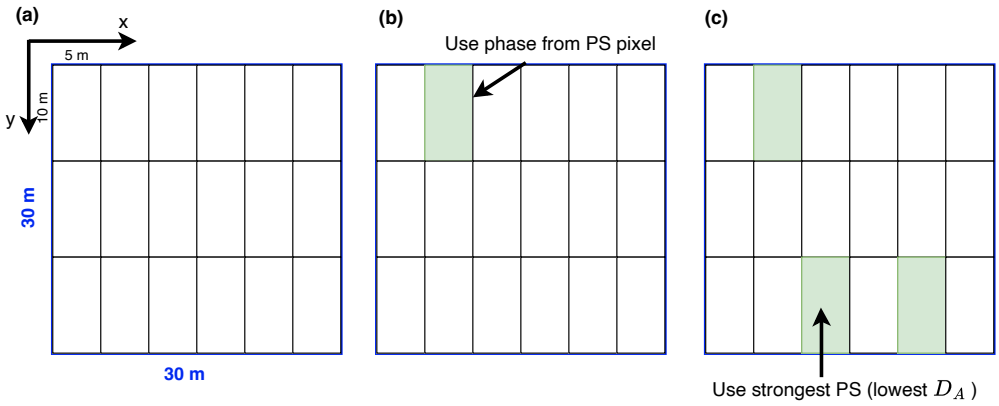

Figure 3: (a) Illustration of one output DISP-S1 pixel compared to input CSLC-S1 grid (b) Output phase selection for the single-PS case (c) Output pixels with multiple PS use the strongest (lowest D_A) phase

The input OPERA CSLC-S1 products, which are a Universal Transverse Mercator (UTM) grid with 5 meter × 10 meter pixels in X- and Y-directions, while the targeted output posting of DISP-S1 products are 30 × 30 meters (Figure 3 (a)). For all DS pixels, we performed the phase linking algorithm on every 6-th and 3-rd pixels in the X- and Y-directions, speeding up the phase linking step by a factor of ∼18 compared to full-resolution phase linking. The PS are estimated directly from the CSLC-S1 products. Since there are 18 full-resolution CSLC pixels are contained within each output interferogram pixel, there are three possible cases for choosing the interferogram phase:

1. The decimation window contains no PS pixels: In this case, the DS phase linking solution is used.

2. One PS is present in the decimation window: In this case the single-reference PS phase is used, regardless of where within the window the PS is located (Figure 3 (b)).

3. Multiple PS pixels are present: Use the phase from the PS with the lowest D_A value (Figure 3 (c)).

Note that while the posting of the output product is 30 x 30 meters, the effective resolution for DS pixels might be larger due to multi-looking during processing. The number of input pixels used within a 100 x 100 meter window varies at each output pixel and is recorded in the statistically homogeneous pixels (SHP) Count image.

The regridded output follows the OPERA DISP-S1 "pixel is area" convention. The "pixel is area" convention uses northing and easting coordinates Y and X, with (0,0) denoting the upper-left corner of the image, and increasing X to the east, increasing Y to the south. The first pixel value fills the grid cell with the top-left position (0,0) and bottom-right position (1,1). The coordinates included in the product refer to the center of the pixel following CF-conventions.

2.9 Creating Stitched Interferograms

The OPERA DISP-S1 product is a frame-based product consisting of a set of CSLC-S1 bursts consecutive along the Sentinel-1 orbit. The OPERA Displacement Frames are defined using the ESA burst ID map [44] such that

- Frames nominally contain 27 bursts (9 bursts along-track, subswaths IW1, 2, and 3 always grouped together)
- The frames overlap by one burst along-track to aid in stitching unwrapped displacement products.
- The DISP-S1 frames are defined on a projected UTM grid, where the UTM zone is determined by the geographic center of the frame.
- The Frames are always on the same geographic grid to ease time series analysis.

After estimating the wrapped phase as described in Section 2.5, the burst-wise interferograms are stitched together into a Frame before phase unwrapping. Any interferograms formed from CSLC-S1 with a different UTM projection are resampled to the Frame projection using sinc interpolation. All interferograms are then merged into a single image, using the data from one of the bursts where overlap exists. Each burst interferogram is eroded by half the size of the multilook search window before merging to ensure that no artifacts occur at burst boundaries.

By default, we create a network of the nearest (in time) three interferograms for each SAR acquisition. Note that since no additional multilooking is performed, the there are no wrapped phase misclosures in the re-formed interferograms; in other words, no additional measurement information is gained, but the phase unwrapping optimization problem often produces fewer errors for short-baseline interferograms.

2.10 Phase Unwrapping

The "true" two-dimensional phase field $\phi[i, j]$ of the interferogram after phase linking is directly related to the line-of-sight slant range changes from the radar to the targets d between the interferometric pair at each point (i, j). However, the phase values are only known modulo 2π since only the principal values of the phase field $\varphi[i, j]$ may be directly measured from the interferogram. The goal of the phase unwrapping step is to reconstruct an estimate $\hat{\phi}[i, j]$ of the true two-dimensional phase field, given its principal values.

Each interferogram in the network is unwrapped independently using the Statistical-cost Network-flow Algorithm for PHase Unwrapping (SNAPHU) [45]. SNAPHU estimates unwrapped phase gradients via Maximum a Posteriori (MAP) estimation using statistical models of interferometric phase, then integrates these gradients to obtain the unwrapped phase surface.

Unwrapping large interferograms presents significant computational challenges. The memory requirements for unwrapping full-resolution Sentinel-1 frames can reach many 10s of gigabytes, often more the available system memory of many modern computers. Since the processing time depends on the quality of the interferometric phase, it can therefore be difficult to predict based only on the size of the interferogram.

A common approach to address this problem is to break the interferogram into smaller tiles, unwrap each tile independently, and reassemble the tiles in a merging step afterward. Since the algorithmic complexity of phase unwrapping algorithms is generally worse than $\mathcal{O}(n)$, breaking the interferogram into smaller tiles tends to improve unwrapping runtime. The memory requirements for unwrapping individual tiles are lower than that needed to process the full interferogram, and multiple tiles can be unwrapped in parallel to improve processing time. The reassembly step involves a secondary correction to address discrepancies in the relative phase between tiles [46, 47].

The DISP-S1 algorithm uses the tiling strategy built into the SNAPHU software [48]. A default of 5×5 tiles are used with 400 pixel overlaps in both the $x-$ and $y-$ direction, and after estimating offsets and reassembling the tiles, a secondary "re-optimization" step is performed, where the entire interferogram is unwrapped. This final step is significantly shorter than using SNAPHU only in single-tile mode, but leads to improvements in regions where the boundaries of tiles experience decorrelation.

The phase unwrapping processor produces two outputs: (1) the unwrapped phase estimate and (2) the connected component labels. The unwrapped phase estimate is an array with the same shape and sample spacing as the original input interferogram and represents the result of tile-based unwrapping at full resolution after applying corrections using the lower-resolution unwrapped results. The phase may be converted to line-of-sight displacement d by the relation

$$d = -\frac{\lambda}{4\pi}\phi, \tag{17}$$

where λ is the radar wavelength. The sign convention is chosen such that positive values of

d indicate apparent displacement towards the satellite and negative values indicate motion away from the satellite.

The connected component labels are an integer-valued array with the same shape as the unwrapped phase. Each connected component is a contiguous region of points in the unwrapped phase that is believed to be free of relative phase unwrapping errors. Connected components are assigned unique positive integer labels, and unreliable unwrapped phase values are assigned a label of 0.

2.11 Time series inversion

After obtaining wrapped phases from phase linking, we unwrap the phase to recover the continuous deformation signal. Although regions which maintain long-term coherence may successfully unwrap single-reference interferograms using a PS-like strategy, most areas show stronger performance using a network of shorter temporal baseline interferogams. By default, we create a network of $M = 3N - 6$ interferograms using a nearest-3 neighbor network. We note again that since no additional multilooking is performed, there are no wrapped phase misclosures in the re-formed interferograms; in other words, no additional measurement information is gained, but the phase unwrapping optimization problem often produces fewer errors for short-baseline interferograms.

The unwrapped interferogram network is inverted to derive phase time series at each SAR acquisition date. At each pixel, the unwrapped phase vector $\mathbf{b} \in \mathbb{R}^{N_{\text{ifg}}}$ can be written as

$$\mathbf{b} = A\mathbf{x} + 2\pi\mathbf{k}_{\text{error}}, \tag{18}$$

where $A \in \mathbb{R}^{N_{\text{ifg}} \times (N-1)}$ is the network incidence matrix, $\mathbf{x} \in \mathbb{R}^{N-1}$ contains correct unwrapped phase values at each date (relative to the first date), and $\mathbf{k}_{\text{error}} \in \mathbb{Z}^{N_{\text{ifg}}}$ is the vector of integer ambiguities from unwrapping errors (which is all 0 in the case of perfectly unwrapped interferograms).

To reduce the impact of phase unwrapping errors, we minimize using the L_1 norm rather than least squares:

$$\underset{\mathbf{x}}{\text{minimize}} \quad \|A\mathbf{x} - \mathbf{b}\|_1.$$

This promotes a sparse residual vector and is more robust to unwrapping outliers than L_2 minimization. While L_1 minimization does not guarantee integer-multiple ($2\pi k$) residuals, it often produces equivalent solutions for pixels with low percentages of unwrapping errors [49, 50].

We solve this optimization problem using the Alternating Direction Method of Multipliers (ADMM) [51], which is computationally efficient for this problem structure. Since the matrix A is identical for all pixels, the Cholesky factorization of $A^T A$ can be precomputed once and reused, significantly reducing computational cost. Pixels and/or dates with

residuals significantly different from $2\pi k$ can be masked as unreliable due to unwrapping errors using the "timeseries inversion residuals" product layer.

2.12 Forward Processing Mode

The DISP-S1 algorithm can be used on either an existing historical archive (known as "Historical mode", where an output DISP-S1 product is created for each of the $M = 15$ input dates, where M number of images in the mini-stack), or may be used to process one new incremental image in near-real time ("Forward mode"). However, since the total runtime of the method is dominated by phase unwrapping, unwrapping a full network of $3M - 6$ interferograms is inefficient. To provide a speed-up to the phase unwrapping and inversion steps for forward processing, a modified, smaller network of interferograms may be unwrapped.

It is known that unwrapping one new, nearest-neighbor interferogram will accumulate errors when cumulatively summed [34] and using only short-temporal baseline interferograms may lead to a biased displacement estimate [41]. Thus, we use all K compressed CSLCs and M real CSLCs to estimate an optimized wrapped phase, but only unwrap the portion of the nearest-3 network which touches the newest acquisition. Compared to the full network of 42 interferograms when $M = 15$, the 6 unwrapping interferograms containing the four most recent dates runs in 10-20% of the time.

Since interferograms containing the first acquisition in the mini-stack are not unwrapped in Forward mode, new displacement outputs are relative to the second-to-last date (which is assumed to have been processed in a previous run). Output products can be combined with previously-archived displacement products to create a longer displacement time-series. To verify that our Forward mode processing produces results consistent with Historical mode, we reprocessed 60 acquisitions from late 2017 to early 2019 that covered the Kilauea eruption using both approaches [52]. We observe similar accuracy in our Forward mode as the Historical mode processing when validated against GPS

2.13 Reference Point Selection

For the DISP-S1 product, the reference point is selected independently for each processing run which is not guaranteed to have zero deformation due to the automated nature of the processing. All pixels inside the largest unwrapping connected component with $\gamma_t > 0.95$ for the ministack are selected. We choose the pixel nearest to the centroid of this region. The process is designed to selected low-noise reference point which is in stable, contiguous area of high coherence, rather than being an outlier PS pixel at the frame boundary.

Note that because no external calibration is used, the displacement results are relative, not an absolute.

2.14 Corrections

The DISP-S1 algorithm generates phase correction layers for the contributions from excess phase delay through the ionosphere and from solid earth tides in addition to the unwrapped phase. These corrections are not applied to the output product by default; users who wish to apply these corrections may subtract the correction from the displacement layer.

2.14.1 Ionospheric Corrections

Earth's ionospheric can introduce phase distortions due to the presence of free electrons in the Earth's ionosphere. These free electrons are created through the ionization of atmospheric molecules primarily due to solar radiation. The density of these electrons varies with altitude and also fluctuates with time and geographical location due to factors such as solar activity, the Earth's magnetic field, and atmospheric conditions. The group delay caused by the propagation through the ionosphere is dependent on the Total Electron Content (TEC) and the radar carrier frequency.

The single-path absolute ionospheric delay along the radar LOS direction, r_{iono} can be approximated to first order as

$$r_{iono} = \frac{K}{f_0^2} \cdot \text{TEC} \tag{19}$$

where $K = 40.31 m^2 s^{-2}$ is a constant, f_0 is the radar center frequency, and TEC is the number of free electons in a 1 m^2 cross section along the slant range from the ground to the radar sensor. Using the thin-shell assumption of the effective ionosphere [53], the TEC at the point where the radar LOS vector intersects with the ionospheric shell can be calculated from the vertical TEC products derived from dual-frequency global navigation satellite system (GNSS) products [53]. The ionospheric delay, denoted as δr, is calculated for each displacement map relative to its corresponding reference date, as expressed by the equation:

$$\delta r_{iono} = r_{iono}^{t} - r_{iono}^{t_{ref}} \tag{20}$$

where, t represents the acquisition time of the displacement product, while t_{ref} denotes the reference time to which the displacement product is referenced.

2.14.2 Solid Earth Tides

Solid Earth Tides (SET) refer to the Earth's deformation caused by the gravitational pull of the Sun and the Moon. The vertical component of these tides typically causes displacement of around ±20 cm, while the horizontal component can lead to displacements up to ±5 cm [54]. The displacements along the east, north, and vertical directions (denoted r_{SET}^{e}, r_{SET}^{n}, and r_{SET}^{v}, respectively) due to these tides are well understood, and they can be calculated

with an accuracy of ∼1 mm. The displacement from SET in the ENU frame can be projected onto the radar LOS as

$$r_{\text{SET,LOS}} = -r^e_{SET}\hat{u}_e + r^n_{SET}\hat{u}_n - r^v_{SET}\hat{u}_v \tag{21}$$

where $[\hat{u}_e, \hat{u}_n, \hat{u}_v]$ are the east, north, and vertical components of the LOS unit vector. To compute a phase correction for each displacement output, $r_{\text{SET,LOS}}$ is calculated for both SAR acquisitions and differenced. Note again that the product sign convention is positive towards the platform, as per the equation.

2.15 Reference Date Selection

The DISP-S1 algorithm outputs a displacement product for each acquisition date relative to a reference date. The reference date moves forward in time as the processing progresses to simplify required inputs to the production data system. This tradeoff occurs because 1. The size of the inputs should not grow indefinitely as the archive grows. 2. Forming long temporal-baseline interferograms leads to decorrelation, unwrapping errors, and low-quality displacement products. 3. Relying on recently-produced displacement products as inputs to new displacement products significantly complicates the near-real-time production system.

To balance trade-offs, the algorithm uses the most recent CSLC and compressed CSLC products as input and moves the reference date forward in time. As a result, users who wish to reconstruct the full time series from the beginning of the Sentinel-1 archive must sum multiple DISP-S1 products. The reference date for each product can be inferred from the product name (as the first timestamp) and from the metadata "/identification/reference_datetime".

2.16 Pixel mask layer

The DISP-S1 product contains multiple quality layers (Section 2.7) which end users may ingest to hide lower quality pixels according to their application. To help less experienced users view the displacement products, a “recommended mask” layer has been added. The mask is a binary image (pixel values may be 1 or 0), where “bad” pixels are marked with 0. A pixel is marked “bad“ if the pixel is marked as a water pixel in the input water mask, or if *both* the temporal coherence and phase similarity are below a threshold (recorded in the product metadata). Note that the mask is an attempt to provide an easy to use quality mask; the choice of thresholds may not hide all low-quality pixels, and certain valid results may be masked.

2.17 Spatial filtering for visualization

The DISP-S1 products contain the unwrapped phase, converted to line of sight displacement in meters, with separate optional correction layers. No temporal or spatial filtering is

performed on the primary output layer. Since atmospheric noise can be as large as 10-20 cm over typical SAR scene scales (100-300 km) [55, 56, 57, 58], this noise often dominates the signal in regions with small deformation, exceeding the magnitude of actual surface displacement.

To visualize the DISP-S1 products at scale, a separate "short wavelength displacement" layer has been created which attempts to remove long-wavelength noise and allow an easy, continuous mosaic of average displacement velocity. The filtered displacement layer is created

1. Mask low coherence pixels using the "recommended mask" (Section 2.16)
2. Fill the gaps from the mask using a nearest neighbor interpolation
3. Create a low pass filtered version of the displacement, using a Gaussian Kernel approximately 30 kilometers in width; subtract the low pass filter result from the original to keep only high pass spatial results
4. Re-apply the recommended mask to hide low quality, interpolated pixels

Note that this simple filtering result removes most of the long-wavelength atmospheric noise ($>$ 30 km), but high-frequency atmospheric noise will remain in the filtered layer. A benefit of the short-wavelength visualization layer is that no reference point need be chosen automatically for all DISP-S1 frames; the low pass filter acts as a "virtual reference point" [59]. However, large-scale deformation features, such as the subsidence bowl in Central Valley, CA [60] will be distorted (or removed, if the feature is larger than 20-30 kilometers in spatial extent).

2.18 Algorithm Inputs

The main inputs to the algorithm are the latest m CSLC-S1 products for the 27 Burst IDs comprising the displacement frame. Additionally, the most recent 5 compressed CSLCs are inputs to the algorithm, which contain the phase information from previous processing runs (used for phase linking), the mean amplitude for the CSLCs used, and the amplitude dispersion (saved as an extra raster band). The mean amplitude and amplitude dispersion are used for PS and DS selection (Section 2.3 and 2.4).

The algorithm also uses a water distance mask to create a binary mask of regions with long-term water. The mask is used to speed up phase unwrapping by skipping decorrelated regions.

At the corrections stage (Section 2.14), the GNSS based ionospheric TEC model is used for each input date to create the excess phase delay caused by propagation through the ionosphere. The CSLC-S1 Static Layer products, containing the line-of-sight unit vectors, are used at this stage to project the zenith delays onto the line-of-sight.

2.19 Algorithm Outputs

The output of the displacement algorithm is the estimated displacement product for the latest acquisition date relative to a reference date over one frame. The displacement product is estimated relative to an arbitrary coherent pixel in the frame, which is not guaranteed to have zero deformation due to the automated nature of the processing.

Additionally, the algorithm also produces a compressed CSLC of the latest ministack which may be archived and used for future processing. During historical mode, the compressed CSLC is archived for each run; during forward mode, this is done every m processing runs.

3 Algorithm Assumptions

3.1 Input coregistered SLC

An important assumption of the algorithm is that the input CSLCs are precisely coregistered. Significant misregistration decorrelates the interferometric phase and degrades the quality of the displacement products. Possible azimuth misregistration, leads to interferometric phase discontinuity at overlap areas between consecutive bursts.

3.2 Static DEM

The CSLC-S1 products are produced with an assumption that the DEM used to produce the geocoded SLCs remains static, and that any update to the DEM may require reprocessing the archive. The DISP-S1 product also assumes that large deviations from the starting DEM will not be corrected in an automatic fashion, but may require a reprocessing after manual identification.

3.3 Missing burst IDs

The algorithm requires CSLC-S1 stacks to maintain consistent temporal and spatial coverage. To achieve this, we analyzed each frame to identify and exclude burst IDs or acquisition dates that would compromise consistency. Figure 4 illustrates an example frame showing burst ID coverage over time, where orange indicates present data and blue indicates missing data.

We evaluate three exclusion strategies for all frames that can be described as follow for Figure 4:

1. Exclude sparse burst IDs: Remove all burst IDs with incomplete temporal coverage, retaining only the bottom three bursts that have consistent acquisition dates.

2. Exclude incomplete dates: Remove all acquisition dates that are missing one or more burst IDs, retaining only dates with full spatial coverage across all bursts.

3. Hybrid approach: Remove the three topmost bursts and all remaining dates with incomplete burst ID coverage (shown in blue in Figure 4).

The optimal strategy was selected based on maximizing both spatial extent and temporal depth subject to having a consistent spatial pattern for every date. In the case of Figure 4, data within the red box are kept and the rest are excluded.

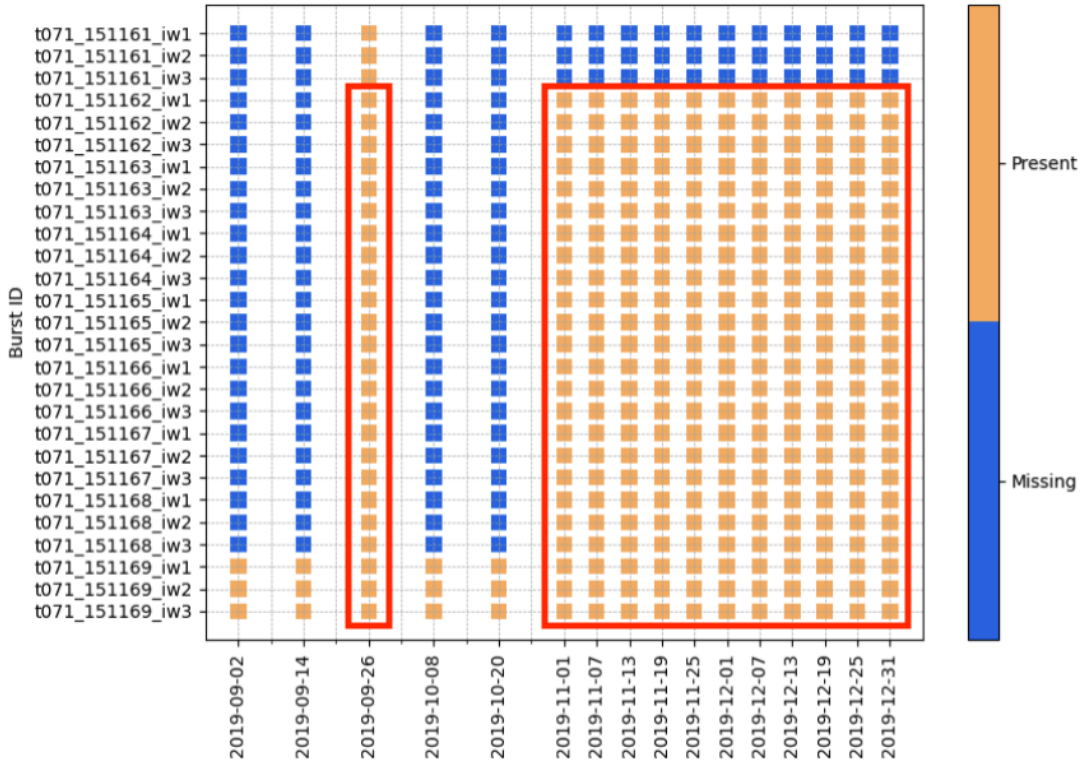

Figure 4: Example frame showing burst ID temporal coverage. Orange cells indicate available data; blue cells indicate missing data. The x-axis represents acquisition dates, and the y-axis represents burst IDs. The red boxes show the burst IDs and dates that we keep.

3.4 Excluding CSLC-S1 acquisitions during winter and rainy season for northern latitudes

The algorithm assumes that at northern latitudes during winter months, the automated InSAR processing will fail due to changes in the scattering surface from snowpack and frozen ground processes [61, 62, 63, 64]. To reduce the impact of seasonal snow and ice on OPERA DISP-S1 northern latitude processing, we implemented a "snow blackout" strategy to systematically exclude winter acquisitions.

We used the National Oceanic and Atmospheric Administration's (NOAA) Global Ensemble Forecast System (GEFS) reanalysis data spanning the past five years, focusing on the 2 meter (the height of the measurement above the Earth's surface) air temperature and categorical surface snow cover [65, 66].

Data were aggregated to a weekly average. A pixel was flagged as "bad" for that week if either the weekly average temperature was below $-2°$C, or the pixel had 4 or more days of snow cover during the week. For each DISP-S1 frame, a week was considered unusable if more than 50% of the frame's pixels were flagged as "bad."

For each frame, weekly "exclusion" flags were generated for each grid cell of the GEFS model for the 5-year period from July, 2020 to July, 2025. The flags were joined to the DISP-S1 frame locations to estimate a single blackout start and end date to be used each year in production. Since the five years contain variability, three candidate blackout strategies were defined:

1. Shortest blackout period: latest observed onset of winter and earliest observed spring melt were used as the start and end dates.

2. Longest blackout period: earliest observed onset of winter and latest observed melt.

3. Median onset and melt dates across the five years.

The median strategy was selected as the default for the majority of frames. If the median blackout exceeded a threshold duration or 210 days ($\sim$ 7 months) for a given frame, the shorter blackout period was used for that frame to retain more data. Frames containing high-priority volcanoes identified in the 2018 USGS National Volcanic Threat Assessment [67] were assigned the conservative strategy (second approach) to ensure that snow-covered volcanic summits were excluded even if surrounding lowlands were snow-free. For example, over the Three Sisters volcano (Frame 30710), the blackout period begins on November 3rd and ends on May 15th, resulting in exclusion of all acquisitions within that range. The downside of this approach is that, some of the frames which rarely have snow but have snow covered volcanic summits, are impacted by the volcano mask.

In addition to excluding winter periods with snow, the rainiest 4-month period (August, September, October, and November) for Central America was excluded due to strong decorrelation observed from heavy vegetation and moisture changes.

Figure 5 provides a summary of blackout (as a duration, in days) for the ascending frames. Descending frames follow similar patterns.

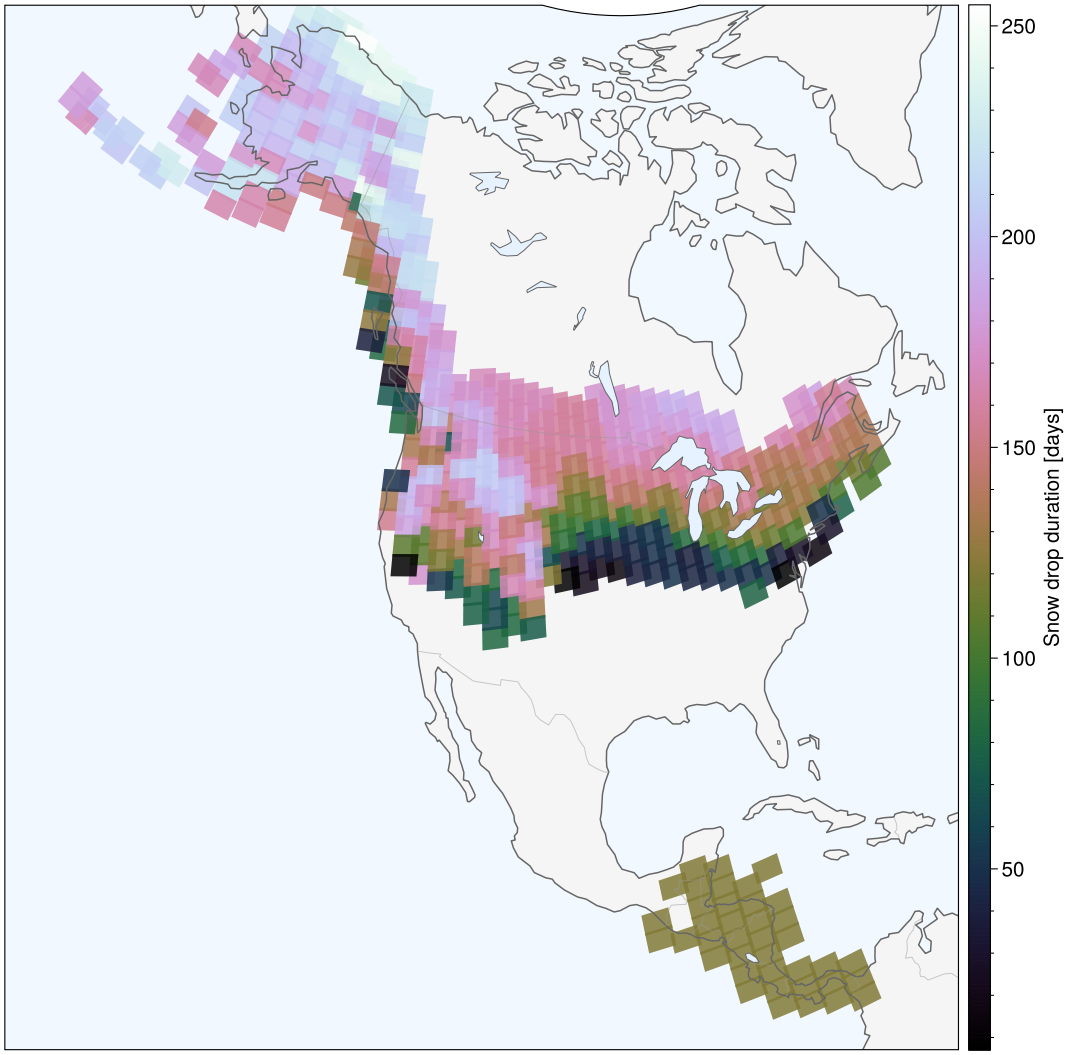

Figure 5: Snow/rain drop durations (in days) of excluded time periods for ascending frames. Winter months are excluded northern latitudes, and rainy months (Aug. – Nov.) are excluded for Central America.

4 Algorithm Implementation

The OPERA DISP-S1 product workflow is developed by the OPERA Algorithm Development Team (ADT). It is implemented in Python and it is open-source accessed through "Dolphin" GitHub repository at `https://github.com/isce-framework/dolphin` [68]. The Science Algorithm Software (SAS), which leverages Dolphin to generate the products, is available at `https://github.com/opera-adt/disp-s1`.

5 Algorithm Usage Constraints

The DISP-S1 algorithm does not account for

- Phase jumps between bursts caused by along-track phase gradients ionosphere phase gradients. The ionospheric correction layer is a range-only correction. Note that none of the correction layers are applied to the displacement layer.
- Phase errors causes by errors in the DEM. Interferograms contain a phase proportional to the perpendicular baseline and the error between the DEM used for processing and the true topographic height. Additionally, the DEM used to create the input CSLC-S1 products is static and does not account for major changes to the Earth's surface, e.g., collapse of the caldera of a volcano.

6 Data Access

Data Access for input data:

- The primary input data to generate the DISP-S1 products, are the CSLC-S1 products which are available through the NASA Alaska Satellite Facility (ASF)-Distributed Active Archive Center (DAAC).
- The Copernicus DEM GLO-30 data are available for download through the Copernicus Data Space Ecosystem (CDSE) at: https://dataspace.copernicus.eu/explore-data/data-collections/copernicus-contributing-missions/collections-description/COP-DEM

Output data Access:

- DISP-S1 products are available through the ASF DAAC.
- The "short-wavelength" displacement is viewed in the Displacement Portal on the ASF DAAC at `https://displacement.asf.alaska.edu/`

7 Contacts

Scott Staniewicz
Jet Propulsion Laboratory, California Institute of Technology
Pasadena, CA, USA
scott.j.staniewicz@jpl.nasa.gov

Sara Mirzaee
Jet Propulsion Laboratory, California Institute of Technology
Pasadena, CA, USA
sara.mirzaee@jpl.nasa.gov

Heresh Fattahi
Jet Propulsion Laboratory, California Institute of Technology
Pasadena, CA, USA
heresh.fattahi@jpl.nasa.gov

References

[1] D. Massonnet and K. L. Feigl, "Radar interferometry and its application to changes in the Earth's surface," *Reviews of Geophysics*, vol. 36, no. 4, pp. 441–500, Nov. 1998.

[2] Y. Fialko, "Interseismic strain accumulation and the earthquake potential on the southern san andreas fault system," *Nature*, vol. 441, no. 7096, pp. 968–971, 2006.

[3] J. Biggs and T. J. Wright, "How satellite InSAR has grown from opportunistic science to routine monitoring over the last decade," *Nature Communications*, vol. 11, no. 1, p. 3863, Aug. 2020.

[4] E. Hussain, A. Hooper, T. J. Wright, R. J. Walters, and D. P. Bekaert, "Interseismic strain accumulation across the central north anatolian fault from iteratively unwrapped insar measurements," *Journal of Geophysical Research: Solid Earth*, vol. 121, no. 12, pp. 9000–9019, 2016.

[5] R. Bürgmann, P. A. Rosen, and E. J. Fielding, "Synthetic Aperture Radar Interferometry To Measure Earth'S Surface Topography and Its Deformation," *Annu. Rev. Earth Planet. Sci*, vol. 28, pp. 169–209, 2000.

[6] D. Massonnet, M. Rossi, C. Carmona, F. Adragna, G. Peltzer, K. Feigl, and T. Rabaute, "The displacement field of the Landers earthquake mapped by radar interferometry," *Nature*, vol. 364, no. 6433, pp. 138–142, Jul. 1993.

[7] Y. Okada, "Surface deformation due to shear and tensile faults in a half-space," *Bulletin of the Seismological Society of America*, vol. 75, no. 4, pp. 1135–1154, 1985.

[8] T. J. Wright, B. E. Parsons, and Z. Lu, "Toward mapping surface deformation in three dimensions using InSAR," *Geophysical Research Letters*, vol. 31, no. 1, 2004.

[9] D. Dzurisin, *Volcano Deformation: Geodetic Monitoring Techniques*. Berlin, Germany: Springer Science & Business Media, 2007.

[10] D. L. Galloway and T. J. Burbey, "Review: Regional land subsidence accompanying groundwater extraction," *Hydrogeology Journal*, vol. 19, no. 8, pp. 1459–1486, Dec. 2011.

[11] E. Chaussard, S. Wdowinski, E. Cabral-Cano, and F. Amelung, "Land subsidence in central mexico detected by alos insar time-series," *Remote Sensing of Environment*, vol. 140, pp. 94–106, 2014.

[12] P. Liu, Q. Li, Z. Li, T. Hoey, Y. Liu, and C. Wang, "Land subsidence over oilfields in the yellow river delta," *Remote Sensing*, vol. 7, no. 2, pp. 1540–1564, 2015.

[13] S. Grebby, E. Orynbassarova, A. Sowter, D. Gee, and A. Athab, "Delineating ground deformation over the tengiz oil field, kazakhstan, using the intermittent sbas (isbas) dinsar algorithm," *International Journal of Applied Earth Observation and Geoinformation*, vol. 81, pp. 37–46, 2019.

[14] C. Carnec and C. Delacourt, "Three years of mining subsidence monitored by sar interferometry, near gardanne, france," *Journal of Applied Geophysics*, vol. 43, no. 1, pp. 43–54, 2000.

[15] G. Herrera, R. Tomás, J. M. López-Sánchez, J. Delgado, J. J. Mallorquí, S. Duque, and J. Mulas, "Advanced dinsar analysis on mining areas: La union case study (murcia, se spain)," *Engineering Geology*, vol. 90, no. 3-4, pp. 148–159, 2007.

[16] H. K. Gupta, "A review of recent studies of triggered earthquakes by artificial water reservoirs with special emphasis on earthquakes in koyna, india," *Earth-Science Reviews*, vol. 58, no. 3-4, pp. 279–310, 2002.

[17] P. Talwani and S. Acree, "Pore pressure diffusion and the mechanism of reservoir-induced seismicity," *Pure and Applied Geophysics*, vol. 122, no. 6, pp. 947–965, 1985.

[18] NASA Jet Propulsion Laboratory, "Opera: Observational products for end-users from remote sensing analysis," https://www.jpl.nasa.gov/go/opera/, n.d., accessed: 2025-10-02.

[19] H. Fattahi, D. P. Bekaert, V. Brancato, Z. Yunjun, Z. Lu, M. G. Bato, J. W. Kim, S. Jeong, K. Liang, and S. Sangha, "Opera coregistered single look complex products from sentinel-1 data," in *AGU Fall Meeting Abstracts*, vol. 2022, 2022, pp. G45A–03.

[20] NASA Earthdata, "NASA Support for SNWG Management Office," https://www.earthdata.nasa.gov/about/nasa-support-snwg/management-office, 2025, accessed: 2025-01-14.

[21] H. A. Zebker and J. Villasenor, "Decorrelation in interferometric radar echoes," *IEEE Transactions on Geoscience and Remote Sensing*, vol. 30, no. 5, pp. 950–959, 1992.

[22] A. Ferretti, C. Prati, and F. Rocca, "Permanent Scatters in SAR Interferometry," *IEEE Transactions on Geoscience and Remote Sensing*, vol. 39, no. 1, pp. 8–20, 2001.

[23] P. Berardino, D. Fornaro, R. Linari, and E. Sansosti, "A New Algorithm for Surface Deformation Monitoring Based on Small Baseline Differential SAR Interferograms," *IEEE International Geoscience and Remote Sensing Symposium*, vol. 2, no. 11, pp. 1237–1239, 2002.

[24] A. Hooper, D. Bekaert, K. Spaans, and M. Arıkan, "Recent advances in SAR interferometry time series analysis for measuring crustal deformation," *Tectonophysics*, vol. 514–517, pp. 1–13, Jan. 2012.

[25] M. Crosetto, O. Monserrat, M. Cuevas-González, N. Devanthéry, and B. Crippa, "Persistent Scatterer Interferometry: A review," *ISPRS Journal of Photogrammetry and Remote Sensing*, vol. 115, pp. 78–89, 2016.

[26] R. Lanari, O. Mora, M. Manunta, J. J. Mallorquí, P. Berardino, and E. Sansosti, "A small-baseline approach for investigating deformations on full-resolution differential sar interferograms," *IEEE Transactions on Geoscience and Remote Sensing*, vol. 42, no. 7, pp. 1377–1386, 2004.

[27] D. A. Schmidt and R. Bürgmann, "Time-dependent land uplift and subsidence in the Santa Clara valley, California, from a large interferometric synthetic aperture radar data set," *Journal of Geophysical Research: Solid Earth*, vol. 108, no. B9, 2003.

[28] A. M. Guarnieri and S. Tebaldini, "Hybrid cramer-rao bounds for crustal displacement field estimators in SAR interferometry," *IEEE Signal Processing Letters*, vol. 14, no. 12, pp. 1012–1015, 2007.

[29] ——, "On the exploitation of target statistics for SAR interferometry applications," *IEEE Transactions on Geoscience and Remote Sensing*, vol. 46, no. 11, pp. 3436–3443, Nov. 2008.

[30] A. Ferretti, A. Fumagalli, F. Novali, C. Prati, F. Rocca, and A. Rucci, "A new algorithm for processing interferometric data-stacks: SqueeSAR," *IEEE Transactions on Geoscience and Remote Sensing*, vol. 49, no. 9, pp. 3460–3470, 2011.

[31] G. Fornaro, S. Verde, D. Reale, and A. Pauciullo, "CAESAR: An Approach Based on Covariance Matrix Decomposition to Improve Multibaseline–Multitemporal Interferometric SAR Processing," *IEEE Transactions on Geoscience and Remote Sensing*, vol. 53, no. 4, pp. 2050–2065, Apr. 2015.

[32] H. Ansari, F. De Zan, and R. Bamler, "Efficient Phase Estimation for Interferogram Stacks," *IEEE Transactions on Geoscience and Remote Sensing*, vol. 56, no. 7, pp. 4109–4125, Jul. 2018.

[33] ——, "Sequential Estimator: Toward Efficient InSAR Time Series Analysis," *IEEE Transactions on Geoscience and Remote Sensing*, vol. 55, no. 10, pp. 5637–5652, Oct. 2017.

[34] S. Mirzaee, F. Amelung, and H. Fattahi, "Non-linear phase linking using joined distributed and persistent scatterers," *Computers & Geosciences*, vol. 171, p. 105291, Feb. 2023.

[35] A. Hooper, H. Zebker, P. Segall, and B. Kampes, "A new method for measuring deformation on volcanoes and other natural terrains using InSAR persistent scatterers: A NEW PERSISTENT SCATTERERS METHOD," *Geophysical Research Letters*, vol. 31, no. 23, Dec. 2004.

[36] P. S. Agram, "Persistent Scatterer Interferometry in Natural Terrain," Ph.D. dissertation, 2010.

[37] A. Parizzi and R. Brcic, "Adaptive InSAR Stack Multilooking Exploiting Amplitude Statistics: A Comparison Between Different Techniques and Practical Results," *IEEE Geoscience and Remote Sensing Letters*, vol. 8, no. 3, pp. 441–445, May 2011.

[38] S. S. Wilks, "The Large-Sample Distribution of the Likelihood Ratio for Testing Composite Hypotheses," *The Annals of Mathematical Statistics*, vol. 9, no. 1, pp. 60–62, Mar. 1938.

[39] I. C. F. Ipsen, "Computing an Eigenvector with Inverse Iteration," *SIAM Review*, vol. 39, no. 2, pp. 254–291, Jan. 1997.

[40] F. D. Zan, F. Rocca, and A. Rucci, "Ps Processing with Decorrelating Targets," p. 5, Apr. 2007.

[41] H. Ansari, F. D. Zan, and A. Parizzi, "Study of Systematic Bias in Measuring Surface Deformation With SAR Interferometry," *IEEE Transactions on Geoscience and Remote Sensing*, vol. 59, no. 2, pp. 1285–1301, Feb. 2021.

[42] N. Cao, H. Lee, and H. C. Jung, "Mathematical Framework for Phase-Triangulation Algorithms in Distributed-Scatterer Interferometry," *IEEE Geoscience and Remote Sensing Letters*, vol. 12, no. 9, pp. 1838–1842, Sep. 2015.

[43] K. Wang and J. Chen, "Accurate Persistent Scatterer Identification Based on Phase Similarity of Radar Pixels," *IEEE Transactions on Geoscience and Remote Sensing*, vol. 60, pp. 1–13, 2022.

[44] SAR-MPC Service, "Sentinel-1 burst ID map," [Online], 2022, version 20220530. [Online]. Available: https://sar-mpc.eu/test-data-sets/

[45] C. W. Chen and H. A. Zebker, "Two-dimensional phase unwrapping with use of statistical models for cost functions in nonlinear optimization," *JOSA A*, vol. 18, no. 2, pp. 338–351, Feb. 2001.

[46] M. T. Calef, K. M. Olsen, and P. S. Agram, "Merging point data for insar deformation processing," *arXiv preprint arXiv:2405.06838*, 2024.

[47] G. Carballo and P. Fieguth, "Hierarchical network flow phase unwrapping," *IEEE Transactions on Geoscience and Remote Sensing*, vol. 40, no. 8, pp. 1695–1708, Aug. 2002.

[48] C. Chen and H. Zebker, "Phase unwrapping for large SAR interferograms: Statistical segmentation and generalized network models," *IEEE Transactions on Geoscience and Remote Sensing*, vol. 40, no. 8, pp. 1709–1719, Aug. 2002.

[49] T. R. Lauknes, H. A. Zebker, and Y. Larsen, "InSAR Deformation Time Series Using an $_1$ -Norm Small-Baseline Approach," *IEEE Transactions on Geoscience and Remote Sensing*, vol. 49, no. 1, pp. 536–546, Jan. 2011.

[50] D. L. Donoho, "Compressed sensing," *IEEE Transactions on Information Theory*, vol. 52, no. 4, pp. 1289–1306, Apr. 2006.

[51] S. Boyd, "Distributed Optimization and Statistical Learning via the Alternating Direction Method of Multipliers," *Foundations and Trends® in Machine Learning*, vol. 3, no. 1, pp. 1–122, 2010.

[52] S. Staniewicz, S. Mirzaee, H. Fattahi, T. Oliver-Cabrera, E. Havazli, G. Gunter, S.-Y. Jeon, M. G. Bato, J. Kim, S. S. Sangha, B. Chapman, A. L. Handwerger, M. Govorcin, P. Agram, and D. Bekaert, "Near-real-time insar phase estimation for large-scale surface displacement monitoring," 2025. [Online]. Available: https://arxiv.org/abs/2511.12051

[53] Z. Yunjun, H. Fattahi, X. Pi, P. Rosen, M. Simons, P. Agram, and Y. Aoki, "Range Geolocation Accuracy of C/L-band SAR and its Implications for Operational Stack Coregistration," *IEEE Transactions on Geoscience and Remote Sensing*, pp. 1–1, 2022.

[54] G. Petit and B. Luzum, "(IERS Technical Note; No. 36)," no. 36.

[55] T. R. Emardson, M. Simons, and F. H. Webb, "Neutral atmospheric delay in interferometric synthetic aperture radar applications: Statistical description and mitigation," *Journal of Geophysical Research: Solid Earth*, vol. 108, no. B5, pp. 1–8, 2003.

[56] H. Fattahi and F. Amelung, "InSAR bias and uncertainty due to the systematic and stochastic tropospheric delay," *Journal of Geophysical Research: Solid Earth*, vol. 120, no. 12, pp. 8758–8773, 2015.

[57] S. Staniewicz, J. Chen, H. Lee, J. Olson, A. Savvaidis, R. Reedy, C. Breton, E. Rathje, and P. Hennings, "InSAR Reveals Complex Surface Deformation Patterns Over an 80,000 km2 Oil-Producing Region in the Permian Basin," *Geophysical Research Letters*, vol. 47, no. 21, p. e2020GL090151, 2020.

[58] D. P. Bekaert, R. J. Walters, T. J. Wright, A. J. Hooper, and D. J. Parker, "Statistical comparison of InSAR tropospheric correction techniques," *Remote Sensing of Environment*, vol. 170, pp. 40–47, 2015.

[59] A. Ferretti, "European Ground Motion Service Algorithm Development Theoretical Basis (ADTB)," p. 81, 2022.

[60] M. Govorcin *et al.*, "Variable vertical land motion and its impacts on sea level rise projections," *Science Advances*, vol. 11, no. 5, p. eads8163, 2025.

[61] R. Gens and J. L. Van Genderen, "SAR interferometry–data processing and error sources," *ISPRS Journal of Photogrammetry and Remote Sensing*, vol. 52, no. 2, pp. 135–155, 1996.

[62] S. Zwieback and E. R. J. Rignot, "Snow accumulation inferred from c-band InSAR in west greenland," *IEEE Geoscience and Remote Sensing Letters*, vol. 11, no. 2, pp. 522–526, 2021.

[63] L. Liu and G. Li, "Monitoring seasonal and long-term permafrost deformation using insar," *Remote Sensing of Environment*, vol. 219, pp. 149–179, 2018.

[64] J. Kim, J. A. Coe, P. G. Hatcher, S. S. Sneddon, K. Rinker, B. J. Minsley, P. D'Anzica, R. Twardock, and J. G. Lee, "Satellite interferometry landslide detection and preliminary tsunamigenic plausibility assessment in prince william sound, southcentral alaska," U.S. Geological Survey, Reston, VA, Tech. Rep. 2023-1099, 2023.

[65] National Oceanic and Atmospheric Administration and National Centers for Environmental Prediction, "NCEP Global Ensemble Forecast System (GEFS) Reanalysis," Available from the NOAA/NCEP website, 2021.

[66] Y. Zhou, Y. Zhu, B. Zhang, X. Weng, J. Wang, D. Hou, and X. Ma, "NOAA's new GEFS V12 and its impacts on precipitation prediction," *Weather and Forecasting*, vol. 36, no. 5, pp. 1559–1574, 2021.

[67] J. W. Ewert, A. K. Diefenbach, and D. W. Ramsey, "2018 update to the US Geological Survey national volcanic threat assessment," US Geological Survey, Tech. Rep., 2018.

[68] S. J. Staniewicz, S. Mirzaee, G. M. Gunter, T. Oliver-Cabrera, E. Havazli, and H. Fattahi, "Dolphin: A Python package for large-scale InSAR PS/DS processing," *Journal of Open Source Software*, vol. 9, no. 103, p. 6997, Nov. 2024.

8 Acronyms

AD	Anderson-Darling test
ADMM	Alternating Direction Method of Multipliers
ADT	Algorithm Development Team
ASF	Alaska Satellite Facility
ATBD	Algorithm Theoretical Basis Document
CCG	Circular Complex Gaussian
CED	Classical Eigenvalue Decomposition
CPL	Combined Phase-Linking
CRLB	Cramér-Rao Lower Bound
CSLC	Coregistered Single Look Complex
CSLC-S1	Coregistered Single Look Complex from Sentinel-1
DAAC	Distributed Active Archive Center
DEM	Digital Elevation Model
DISP-S1	Displacement from Sentinel-1
DS	Distributed Scatterer(s)
ECDF	Empirical Cumulative Distribution Function
ECMWF	European Centre for Medium-Range Weather Forecasts
EGMS	European Ground Motion Service
EMI	Eigendecomposition-based Maximum-likelihood estimator of Interferometric phase
ENU	East-North-Up
ESA	European Space Agency
EVD	Eigenvalue Decomposition
GEFS	Global Ensemble Forecast System
GLRT	Generalized Likelihood Ratio Test
GNSS	Global Navigation Satellite System
GPS	Global Positioning System
InSAR	Interferometric SAR

IW	Interferometric Wide (S1-A/B mode)
JPL	Jet Propulsion Laboratory
KS	Kolmogorov-Smirnov test
LOS	Line of Sight
MAP	Maximum a Posteriori
MLE	Maximum Likelihood Estimator
NASA	National Aeronautics and Space Administration
NOAA	National Oceanic and Atmospheric Administration
NRT	Near-Real-Time
OPERA	Operational Product for End-users from Remote sensing Analysis
PS	Persistent Scatterer(s)
RMSE	Root Mean Square Error
SAR	Synthetic Aperture Radar
SAS	Science Algorithm Software
SBAS	Small Baseline Subset
SET	Solid Earth Tides
SHP	Statistically Homogeneous Pixel
SLC	Single-Look Complex
SNAPHU	Statistical-cost Network-flow Algorithm for PHase Unwrapping
TEC	Total Electron Content
USGS	United States Geological Survey
UTM	Universal Transverse Mercator
VTEC	Vertical TEC

9 Acknowledgements

The OPERA Level-2 CSLC-S1 and OPERA Level-3 Displacement from Sentinel-1 products are free and openly available at the ASF DAAC. The DEM used during processing was modified to be a combination of the Copernicus DEM 30-m and Copernicus DEM 90-m models provided by the European Space Agency. The Copernicus DEM 30-m and Copernicus DEM 90-m were produced using Copernicus WorldDEM-30 DLR e.V. 2010-2014 and Airbus Defence and Space GmbH 2014-2018 provided under COPERNICUS by the European Union and ESA; all rights reserved. OPERA, managed by the Jet Propulsion Laboratory and funded by the Satellite Needs Working Group, is creating remote sensing products to address Earth observation needs across U.S. civilian federal agencies. This research was carried out at the Jet Propulsion Laboratory, California Institute of Technology, under a contract with the National Aeronautics and Space Administration (80NM0018D0004).